Entropy Stabilized Medium High Entropy Alloy Anodes for Lithium-ion Batteries

N.B. When citing this work, cite the original published paper.

(article starts on next page)

Entropy Stabilized Medium High Entropy Alloy Anodes for Lithium-ion Batteries

Sajid Alvi,*[a] Ashley P. Black,[b] Ignacio Jozami,[a] Carlos Escudero,[c] Farid Akhtar,[d] and Patrik Johansson[a, e]

One often proposed route to improved energy density for lithium-ion batteries is to use alloy anodes, such as silicon, able to store large amounts of lithium. Mechanical instability caused by the large expansion and contraction associated with (de)lithiation, and hence bad cyclability, has, however, so far hindered progress. As proof-of-concept of a remedy, we here present BiSbSe$_{1.5}$Te$_{1.5}$, a medium high-entropy alloy with improved cycling stability for conversion-alloying (de)lithiation

reactions. We attain five to twenty times more stable cycles than previously reported for comparable metal-Se and -Te-based anodes, with a very good reversible capacity (464 mAh g^{-1}) for up to 110 cycles- and this without using any carbonaceous materials to create a composite. Altogether, this highlights how alloy engineering and increased entropy materials can stabilize conversion-alloying electrodes.

Introduction

The transition from fossil fuel driven to electrified mobility has accelerated the need for energy storage devices with higher energy density. Lithium-ion batteries (LIBs), in particular, have attained popularity due to their high energy density and stable cycling, with numerous cathode chemistries both researched and employed.[1] Comparatively, much fewer anodes have been put forth, and the commonly employed graphite anode, at 372 mAh g^{-1} theoretical capacity, in practice limits the cell energy density and furthermore also exhibits issues associated with lithium plating at low voltages and sub-ambient temperatures.[2]

Out of the anode materials that *have* been investigated, such as metal oxides,[3] sulfides,[4] selenides,[5] and tellurides,[6] and alloy anodes; the latter based on Si (by far the most common),[7] Sn, Sb, Ge, or Bi, all have large theoretical capacities, but suffer from large volume expansion ($>300\%$) during lithiation, leading to pulverization and unstable solid electrolyte interphases (SEIs).[8–11] Nano-engineering, such as yolk-shell structures or nanowires, can alleviate pulverization, but they require complex synthesis routes, making them difficult and/or expensive for upscaling.[12] The use of binary/ternary alloys employs solid solution strengthening to improve the structural stability during (de)lithiation.[13,14] Recently, metal chalcogenides with high specific capacities have been reported upon,[5,6] which store lithium ions through a conversion reaction, due to weak M–C (M: metal; C: Se, and/or Te) bonds, followed by an alloying reaction depending on available active material (M: Sn, Sb, Ge, *etc*.). Most of the low entropy metallic Se/Te alloys are synthesized as a composite material with carbon, such as Bi$_2$Se$_3$-C, Bi$_2$Te$_3$-C, Sb$_2$Se$_3$-C, Sb$_2$Te$_3$-C, and BiSbTe$_3$-C, in order to enhance the electrical conductivity and reduce self-pulverization, adding additional steps to the synthesis routes.[15–19] Amongst the chalcogenide elements, Te is the rarest element, but a by-product from other expensive ore, such as gold and copper, and the production has increased with the advancement of the refining processes.[20]

We here make use of the fact that combining multiple lithium alloying elements and conversion chalcogenides can be an efficient way forward, especially when combined with the notion of solid solution strengthening eliminating the afore-mentioned additional composite-creating step.[13] Indeed, recently, high-entropy materials, such as high-entropy oxides, have been explored as anodes where entropic stabilization has been coupled to enhanced cycling performance.[21]

Here, proof-of-concept of enhanced cycling stability during (de)lithiation through increased entropy is made via BiSbSe$_{1.5}$Te$_{1.5}$ (BSST), a medium high-entropy alloy (MHEA). An MHEA is defined as an alloy consisting of three to four principal

[a] Dr. S. Alvi, I. Jozami, Prof. P. Johansson
Department of Physics
Chalmers University of Technology
Chalmersplatsen 4, 412 96 Göteborg, Sweden
E-mail: sajid.alvi@chalmers.se

[b] Dr. A. P. Black
Institut de Ciència de Materials de Barcelona, ICMAB-CSIC Campus UAB,
08193 Bellaterra, Catalonia, Spain

[c] Dr. C. Escudero
NOTOS, ALBA Synchrotron
Cerdanyola del Vallès, 08193, Catalonia, Spain

[d] Prof. F. Akhtar
Department of Materials Science and Mathematics
Luleå University of Technology
97187, Luleå, Sweden

[e] Prof. P. Johansson
ALISTORE-ERI
CNRS FR 3104, Hub de l'Energie
80039 Amiens Cedex, France

Supporting information for this article is available on the WWW under https://doi.org/10.1002/batt.202300585

Batteries & Supercaps

Research Article
doi.org/10.1002/batt.202300585

Chemistry
Europe

European Chemical
Societies Publishing

elements, a step on the way to an HEA, being composed of five or more principal elements.[22] BSST is an MHEA that previously has been used in thermoelectric applications,[23] but here its composition combines the large capacities available from the Li alloying elements Bi and Sb with the high electronic conductivity available from the Li conversion chalcogenide elements Se and Te.[5,6,24] Furthermore, we chose Sb_2Te_3 to build a case for the (de)lithiation performance of a low entropy metal chalcogenide *vs.* medium entropy BSST anode. While the other anodes, such as Bi_2Se_3, Bi_2Te_3, and Sb_2Se_3 are of interest, however, it is well documented that they all suffer pulverization merely after a few cycles.[15–17]

Experimental

Synthesis

Powders consisting of Bi (45 μm, 99.5%) and Sb (45 μm, 99.5%) were purchased from GoodFellow Cambridge Ltd. (Huntingdon, England), Se (45 μm, 99.999%) from Thermo Fisher Scientific (MI, USA), and Te (75 μm, 99.99%) from US Research Nanomaterials Inc. (US-nano, Houston, TX, USA). For the MHEA, stoichiometric amounts of Bi, Sb, Se, and Te were milled using 45 ml zirconia jar and zirconia balls (5 mm Ø) with a ball to powder ratio of 20:1. The ball milling was performed under argon atmosphere for 10 h with 10 min of milling and 30 min cooling steps at 600 rpm using a high-energy planetary ball-miller (Pulverisette 7 Premium line, Fritsch, Germany). For comparison, low entropy Sb_2Te_3 (ST) was also synthesized using stoichiometric amounts of Sb and Te with the same ball milling procedure. The powders were handled in an argon-filled glove box to avoid any oxidation of the metallic powders.

Characterization

Synchrotron X-ray diffraction (SXRD) patterns were collected on the NOTOS beamline (ALBA synchrotron, Cerdanyola del Vallès, Spain) using the position sensitive detector MYTHEN and $\lambda = 1.1272$ Å. The as-prepared BSST powder was embedded in a 0.5 mm Ø borosilicate glass capillary and spun during XRD data collection. X-ray diffraction of as-prepared ST powder was measured using Bruker D8 Discover (Bruker, MA, US). The as-prepared powder morphology and compositional analysis were characterized using scanning electron microscopy (SEM, JEOL JSM-7800F Prime, Japan) equipped with energy-dispersive X-ray spectroscopy (EDX) with an accelerating voltage and working distance of 15 kV and 10 mm, respectively. The cross-section of electrode coated on copper current collector was characterized using SEM equipped with focused-ion beam (FIB, Versa3D, FEI, Hillsboro, Oregon, USA) using accelerating voltage of 30 kV, and two different currents of 15 nA and 1 nA for rough milling and polishing, respectively. Differential scanning calorimetry (DSC) and thermal gravimetric analysis (TGA) were carried out at 5 °C/min from room-temperature up to 800 °C in argon atmosphere using simultaneous thermal analyser (SDT 650, TA Instruments, USA). The melting point temperature analysis was performed using TRIOS software provided by TA instruments.

Operando SXRD was carried out at the NOTOS beamline (ALBA) using a MYTHEN detector and $\lambda = 1.1272$ Å. The experiments were conducted on 2032 coin cells with a 5 mm Ø drilled hole covered by a 75 μm thick Kapton window (KIT Campus Transfer) and a setup enabling alternate sequential measurement of four cells in the same run. Self-standing positive electrodes consisting of BSST,

Super P carbon and polytetrafluoroethylene (PTFE) (70:25:5) of 4 mm Ø and *ca.* 4 mg in weight were used to accommodate higher loadings of active materials sampled by the X-ray beam. A copper foil (8 μm, 99.9%, GoodFellow Cambridge Ltd., England) was placed above the window on the positive electrode side to ensure good electric contact. Thin Cu foil was indispensable to allow sufficient X-ray transmission (40% transmission at 11 keV for 8 μm Cu). Lithium disks of 16 mm Ø and 0.45 mm thick from MTI Corporation (Richmond, CA, USA) were used as counter electrodes. One glass fibre filter disk (420 μm thickness, Whatman, GE Healthcare) was used as separator, and 1 M $LiPF_6$ dissolved in ethylene carbonate (EC) and diethylene carbonate (DEC) (50:50 volume) with 10 wt.% fluoroethylene carbonate (FEC) was used as electrolyte[1]. Cells were cycled between 0.01 to 3.0 V *vs.* Li^+/Li^o using a Biologic VSP potentiostat in galvanostatic mode with potential limitation (GCPL) at a C/10 rate (54 mA g^{-1}). Rietveld refinements and Fourier analysis were carried out with the FullProf suite.[25]

Battery performance tests

The electrodes were prepared by mixing BSST active material (70 wt.%) with Super P carbon (20 wt.%), sodium carboxymethyl cellulose (CMC, 5 wt.%), and styrene butadiene rubber (SBR, 5 wt.%) in deionized water. The slurry was subsequently cast onto copper foil (17 μm, Schlenk Metallfolien GmbH & Co. KG, Germany) and dried at 80 °C in a vacuum oven for 12 h. Electrodes (13 mm Ø) were cut out and further dried in vacuum at 80 °C for 12 hours. The mass loading of active material in the electrode was kept between 1.5–2.0 mg cm^{-2} and coating thickness of *ca.* 16 μm (Figure S1a–b). A similar procedure was carried out to prepare the ST electrodes (Figure S1c–d). Coin cells (CR2030) were assembled in an argon filled glove box using lithium metal (0.2 mm thickness, 12 mm Ø, purity > 99.8%, Honjo Metals) as negative electrode, glass fibre separators (420 μm thickness, Whatman GF/C, GE Healthcare), and electrolytes of 1 M $LiPF_6$ dissolved in EC and ethyl methylene carbonate (EMC) (30:70, by wt.%) with 10 wt.% FEC (E-lyte Innovations GmbH, Münster, Germany) and 1 M $LiPF_6$ dissolved in EC and dimethyl carbonate (DMC) (50:50, by vol%) (Solvionic, Toulouse, France). Galvanostatic discharge/charge cycling (GC) tests were performed between 0.01 to 3 V *vs.* Li^+/Li^o at C/5 (107 mA g^{-1}) and C/20 (26 mA g^{-1}) rates at room temperature (22 °C) using a battery test system (Scribner 585, NC, USA). Cyclic voltammetry (CV) and electrochemical impedance spectroscopy (EIS) were carried out, within same voltage range as the GC, at 0.1 mV s^{-1} and in the frequency range of 1–100 MHz, respectively, using a VSP multi-channel potentiostat-galvanostat (Bio-Logic Science Instruments, Seyssinet-Pariset, France). EIS was performed on the as-assembled coin cells and at the end of each cycle using a C/5 (107 mA g^{-1}) rate.

Results and Discussion

We start by refining the structure of the as-prepared BSST, followed by characterizing its morphology and thermal stability. The electrochemical performance is then evaluated in lithium half-cells, along with the effect of using electrolytes with and without FEC as an additive on the stability of the SEI. The

---

[1] Please note that the *operando* studies used a different binder (due to self-standing electrode), a different coin cell dimension, and a different electrolyte. However, this does not affect the comparisons made or the conclusions drawn.
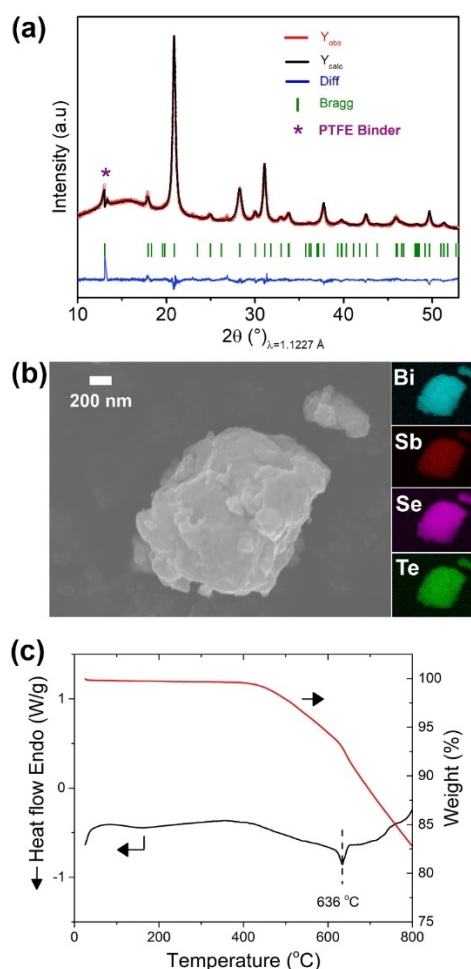
Batteries & Supercaps

Research Article
doi.org/10.1002/batt.202300585

Chemistry Europe
European Chemical
Societies Publishing

Figure 1. The as-prepared BSST electrode: (a) Rietveld refinement of SXRD patterns (details on assignment of the excluded region corresponding to PTFE binder available in Figure S2), (b) SEM micrograph with elemental EDX mapping, and (c) TGA and DSC traces.
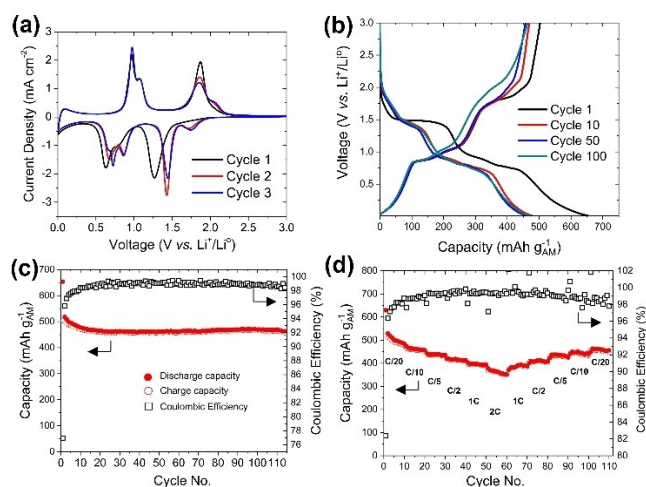

Figure 2. BSST anode half-cell tests: (a) CV (0.1 mV s^{-1}), (b) GC discharge-charge profiles (C/20), (c) GC (C/20), and (d) rate capability.

structural evolution during (de)lithiation is studied using *operando* X-ray diffraction for two cycles, and finally we conduct *post mortem* of our electrodes.

The as-prepared BSST MHEA powder has a rhombohedral crystal structure (space group $R\bar{3}m$), with a = 4.2061(2) Å and c = 29.811(1) Å, and a cell volume of 456.74(2) Å^3 (Figure 1a, Table S1). The powders showed uniform elemental distribution and were stable up to *ca.* 450 °C and fully melts at *ca.* 630 °C, suggesting a single-phase material (Figure 1b–c).[23] The as-prepared ST powders match well with the rhombohedral structure (JCPDS # 71–0393) with a uniform distribution of elements (Figure S3). The particle size of BSST and ST ranges from 0.5 to 20 μm (Figure S4).

The CV of the BSST anode in a half-cell configuration shows three peaks during the first lithiation and de-lithiation in the first cycle (Figure 2a). The first cathodic peak at 1.27 V *vs.* Li$^+$/Li° is due to conversion reactions, forming both Li$_2$Se and Li$_2$Te, and is followed by two peaks at 0.75 and 0.62 V *vs.* Li$^+$/Li° corresponding to both the alloying reactions with Sb to form Li$_3$Sb and Bi to form Li$_3$Bi, respectively, and the formation of the SEIs. The anodic peaks correspond to reversible de-alloying at 0.97 V *vs.* Li$^+$/Li° (Li$_3$Bi) and 1.07 V *vs.* Li$^+$/Li° (Li$_3$Sb), followed by the re-conversion reactions of Li$_2$Se and Li$_2$Te at 1.87 V *vs.* Li$^+$/Li°.[18,26,27] In the subsequent cycles, the cathodic conversion and alloying peaks shift to slightly higher potentials: 1.4 V *vs.* Li$^+$/Li° and 0.68–0.86 V *vs.* Li$^+$/Li°, respectively, while the anodic de-alloying and re-conversion peaks are fixed, suggesting good reversibility. Some irreversibility of the conversion reaction can, however, be observed as reduced intensities. Furthermore, additional peaks, from the second cycle and onwards, appear at 1.74 V (cathodic) and 2.06 V (anodic), which are due to intercalation in the layered crystal structure of BSST, albeit visible in the 1st cycle of differential capacity plot (Figure S5b and S6b), as reported on previously for both Se- and Te-based alloys with hexagonal crystal structures.[28,29]

The GC shows a stable capacity of *ca.* 464 mAh g^{-1} and a coulombic efficiency (CE) of > 99 % (Figure 2b) with contributions from a plateau at 1.5 V to 1.37 V *vs.* Li$^+$/Li° and a two-step plateau 0.96 V to 0.70 V *vs.* Li$^+$/Li°, corresponding to conversion and alloying reactions, respectively.[18,26,27] The conversion reaction is reduced in the subsequent cycles, due to irreversible loss of capacity, which agrees well with the CV (Figure 2a), while the two-step alloying plateau stays the same over 100 cycles, suggesting excellent reversibility. This is corroborated by the differential capacity plots (Figure S5b), where the conversion peaks at the cathodic and anodic side reduce while the alloying peaks increase after 50 cycles. Looking at the first few cycles and then up to the 100th cycle we have a 92.2 % capacity retention (Figure 2c), which is 50–70 % higher than previously reported for alloys containing two or three of the Bi, Sb, Se, and Te elements without carbon compositing and similar to their composites.[19,30,31] However, at higher rates (C/5), the capacity starts to fade after *ca.* 80 cycles (Figure S6a) as compared to 115 cycles at slower rates (C/20) (Figure S5a), which can be related to depletion of the FEC additive.[32] The cycling stability of BSST at C/5 is still better than ST for which the capacity fade starts after the 20th cycle (Figure S7). However, the FEC electro-

Batteries & Supercaps

Research Article
doi.org/10.1002/batt.202300585

Chemistry
Europe
European Chemical
Societies Publishing

lyte additive here used with ST leads to slower capacity decay as compared to previous reports.[18] By *post mortem* analysis of the separator from BSST coin cell was found to be completely dry after 200 cycles, which can be linked to electrolyte consumption to (re−)develop a stable SEI, often quoted to be larger for conversion-alloying anodes.[33–35] Yet the electrode displayed no cracks after 80 and 200 cycles (Figure S8a–d) despite that expansion can be observed (Figure S8b,d). Furthermore, no transfer of electrode material to the separator was noted, suggesting good electrode-current collector adhesion (Figure S8a,c inset). On the other hand, ST electrode showed higher cracks and particle expansion after 80 cycles (Figure S9). The use of an electrolyte without FEC in BSST electrode showed significant capacity fading already after 40 cycles (Figure S10), thus confirming that FEC is crucial for stable SEI formation.[36] The change from DMC to EMC as co-solvent to EC is not considered to play a major role for capacity or SEI formation. Previous works have shown that the use of FEC additive to either EC/DMC or EC/EMC co-solvents participates in the formation of a stable solid electrolyte interphase (SEI), which is crucial in protecting the alloy anode, suppressing dendrite formation, and enhancing ionic conductivity and the cycle life.[36–38] Finally, the rate capability test showed agreeable performance, as compared to e.g. metal-Se or -Te carbon composite based anodes, which is due to its better structural stability and also agreeable CE (Figure 2d).

EIS was applied both to observe the interfacial/charge transfer resistance and to quantify the effect of FEC for stable SEI formation (Figure 3). For the former, the charge transfer resistance was reduced from 222 Ω (fresh cell) to 23 Ω (after the 1st cycle) and then further down to 18 Ω (after the 20th cycle). The cycled EIS showed two semi-circles arising from SEI resistance and charge transfer resistance. The resistance in both cases showed a gradual reduction up to the 15th cycle and then stayed constant until the 20th cycle. This order of magnitude reduction from fresh to 20 cycles in resistance can be related to the formation of a stable SEI, which can further enhance the charge transfer kinetics.[27,28]

The *operando* SXRD (Figure 4a–c) reveals a significant decrease in crystallite size alongside an apparent succession of peak displacements (indicated by arrows) and structural transformations occurring during the first and second discharge and charge cycles. In the early stages of the first discharge, a noticeable shift in the main peaks of the BSST ($R\bar{3}m$) phase towards lower angles is evident (Indicated by black arrows in
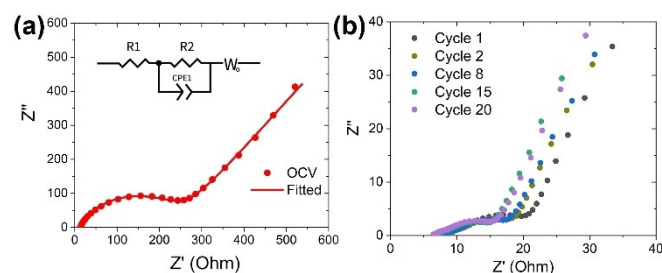

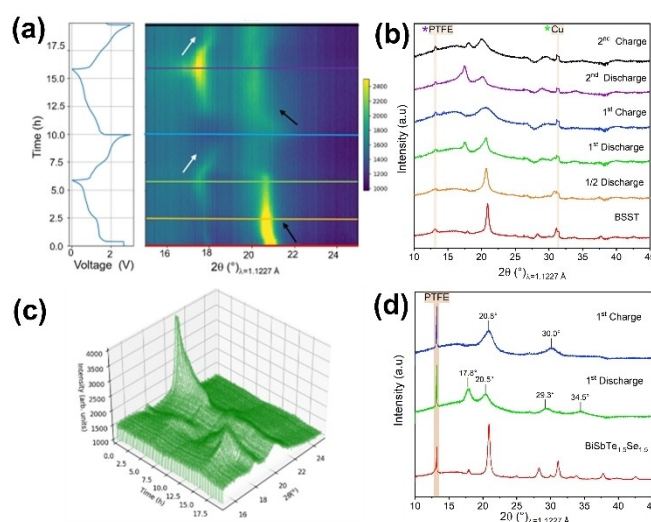
Figure 3. EIS of the BSST MHEA anode.

Figure 4. (a) Characteristic voltage *vs.* time profile for a BSST//Li cell and corresponding *operando* SXRD patterns, coloured lines mark selected patterns represented in (b) and arrows show peak evolution tendencies, (c) zoomed-in 3D image, and (d) XRD patterns at the end of first discharge and charge of *ex situ* data. Purple asterisk at $2\theta = 13.3°$ and green asterisk at $31.3°$ mark excluded regions corresponding to PTFE binder and the Cu current collector, respectively.

Figure 4a). According to Rietveld refinements (Figure S11a–b and Table S1), this shift aligns with approximately a 3% lattice volume expansion, indicating an isostructural lithiation of the BSST ($R\bar{3}m$) structure. As conversion and alloying reactions progress, a significant decline in the peak intensity of the BSST phase is observed, particularly prominent during the latter half of the discharge. Moreover, the phases formed upon cycling display broad peaks with low intensities, indicating small crystal domain sizes. To overcome the challenging phase identification from the *operando* data, complementary *ex situ* data was collected, and their corresponding SXRD displayed in Figure 4d shows the sample corresponding to the end of first discharge with peaks at 17.8°, 20.5°, 29.3°, and 34.5° that are compatible with the peaks that emerge upon discharge in the *operando* data (Figure 4b). The Rietveld refinement of the phase formed at the discharge's final stage, as depicted in Figure S12a, shows a satisfactory agreement with a single cubic ($Fm\bar{3}m$) phase. This phase is isostructural to the lithiated binary compounds Li_3Bi, Li_3Sb, Li_2Se and Li_2Te and its refined lattice parameter is in close agreement with the average lattice parameter of the combination of all four binary lithium compounds (a = 6.4174(7) Å vs a = 6.453 Å) (Figure S13–14 and Table S1). The SXRD data does not suggest any evidence of phase segregation, indicating the maintenance of a medium high-entropy property within the alloy during the first discharge. Resulting in the formation of a single lithiated MHEA ($Li_xBiSbSe_{1.5}Te_{1.5}$) cubic phase.

Upon charge, a shift in the main peaks of the lithiated cubic phase ($Fm\bar{3}m$) is observed (white arrows in Figure 4a), followed by the appearance of new peaks at 20.8° and 30.0°, especially evident in the *ex situ* data depicted in Figure 4d. The shift towards higher Bragg angles of the cubic phase, especially evident after the second charge plateau (1.8 V vs. $Li^+/Li°$), can

be associated to the delithiation of the cubic phase. As the dealloying and re-conversion reactions take place sequentially during charge, the initial shift towards higher Bragg angles is consistent with a decrease in the contribution of "$Li_3(Bi,Sb)$" in the lithiated MHEA. The appearance of new peaks at 20.8° and 30.0° during charging is compatible with the formation of a hexagonal phase with space group P3$_1$21, exhibiting refined lattice parameters (a = 4.285(2) Å and c = 6.554(4) Å) and a cell volume of 104.2(2) Å^3. These lattice parameters do not correspond to those of the pure compounds Bi, Sb, Se, Te (Figure S15 and Table S1), and no additional phase corresponding to single elements or binary alloys have been identified during cycling, suggesting the formation of the new phase compatible with a conservation of MHEA upon charge. The change in polymorphism between the initial material ($R\bar{3}m$), isostructural to Bi and Sb, and the phase recovered at the end of charge (P3$_1$21), isostructural to Se and Te, may be consequent to the stepwise nucleation and growth of the phases formed during the conversion and alloying reactions that take place upon electrochemical cycling. At the end of the second charge, the P3$_1$21 phase is recovered alongside a remaining fraction of the partially lithiated cubic phase with a refined lattice parameter a = 6.211(2) (Figure S12b, Table S1). Remarkably, the second and possibly the subsequent cycles, involve the conversion of a unlithiated BSST MHEA with hexagonal (P3$_1$21) phase to a cubic lithiated (Fm-3 m) phase upon discharge and returning to the hexagonal (P3$_1$21) phase upon charge. Both phases, cubic and hexagonal, permit a certain degree of solid solution in the early stages of each discharge and charge cycle. Furthermore, no additional phases have been identified, suggesting the potential conservation of MHEA throughout cycling.

Operando SXRD analysis aligns well with the proposed mechanism derived from CV and GC data. However, it reveals that the sequential conversion and alloying reactions do not generate individual identifiable phases in SR-XRD. Instead, they form single phases with lattice parameters compatible with both lithiated and unlithiated MHEA compounds. The new phases formed during cycling display broad peaks with low intensities, indicating small crystal domain sizes, further complicating the phase identification, and the possibility of amorphous phases formed and not reflected in the diffractograms cannot be dismissed. Hence, the XRD analysis-derived mechanism might not encompass sub-nanometric or non-crystalline phases potentially occurring during cycling, necessitating further investigation.

Conclusions

The stable specific capacity, good rate capability and coulombic efficiency indicate reduced pulverization arising from solid solution strengthening and entropy stabilisation of the BSST MHEA anode, as compared to previously reported low entropy alloys of similar compositions.[15,18,19,27,30] Furthermore, we achieve a *volumetric* capacity of 3224 mAh cm^{-3} after 100 cycles, almost five times that of graphite and silicon anodes, by virtue of the much higher density (6.95 g cm^{-3}) of BSST.[23,39] The

entropic conservation mechanism during (de)lithiation has been elucidated with the formation of a cubic phase during discharge, followed by formation of a hexagonal phase on charge, which is reversible during the second cycle. Furthermore, we also elucidated the details of the intercalation of lithium ions into BSST, which is scarcely reported in the literature.[28,40] Overall the impact of solid solution strengthening through entropy to solve/reduce the pulverization associated with large expansion and contraction during (de)lithiation in conversion-alloying type anodes is show-cased. Furthermore, the need for additional composite creating steps is avoided reducing the cost and time for upscaling. MHEAs is a move towards using true HEAs, possibly further enhancing the cycling stability.

Supporting Information

Galvanostatic charging of BSST anode at C/5, SEM images of electrode surfaces before and after cycling, additional *operando* XRD analysis data, and particle characterization and galvanostatic charging of Sb_2Te_3.

Conflict of Interests

The authors declare no conflict of interest.

Data Availability Statement

The data that support the findings of this study are available from the corresponding author upon reasonable request.

Batteries & Supercaps

Research Article
doi.org/10.1002/batt.202300585

Chemistry Europe
European Chemical
Societies Publishing

[1] A. Manthiram, *Nat. Commun.* **2020**, *11*, 1–9.
[2] J. Lu, Z. Chen, F. Pan, Y. Cui, K. Amine, *Electrochem. Energy Rev.* **2018**, *1*, 35–53.
[3] S. Fang, D. Bresser, S. Passerini, *Adv. Energy Mater.* **2020**, *10*, 1902485.
[4] S. Wang, C. Qu, J. Wen, C. Wang, X. Ma, Y. Yang, G. Huang, H. Sun, S. Xu, *Mater Chem Front* **2023**, *7*, 2779–2808.
[5] X. Li, J. Qu, Y. Zhao, Q. Lai, P. Wang, *Composites Part B* **2022**, *242*, 110045.
[6] H. Fan, P. Mao, H. Sun, Y. Wang, S. S. Mofarah, P. Koshy, H. Arandiyan, Z. Wang, Y. Liu, Z. Shao, *Mater. Horiz.* **2022**, *9*, 524–546.
[7] P. Zheng, J. Sun, H. Liu, R. Wang, C. Liu, Y. Zhao, J. Li, Y. Zheng, X. Rui, *Batter Supercaps* **2022**, *6*, 202200481.
[8] W. J. Zhang, *J. Power Sources* **2011**, *196*, 13–24.
[9] Y. Jin, B. Zhu, Z. Lu, N. Liu, J. Zhu, *Adv. Energy Mater.* **2017**, *7*, 1700715.
[10] X. Liu, X. Y. Wu, B. Chang, K. X. Wang, *Energy Storage Mater.* **2020**, *30*, 146–169.
[11] A. Wang, W. Hong, L. Yang, Y. Tian, X. Qiu, G. Zou, H. Hou, X. Ji, *Small* **2020**, *16*, 1–23.
[12] N. Mahmood, T. Tang, Y. Hou, *Adv. Energy Mater.* **2016**, *6*, 1600374.
[13] K. Mishra, X. C. Liu, M. Geppert, J. J. Wu, J. T. Li, L. Huang, S. G. Sun, X. D. Zhou, F. S. Ke, *J. Mater. Res.* **2018**, *33*, 1553–1564.
[14] X. Wang, S. Tang, W. Guo, Y. Fu, A. Manthiram, *Mater. Today* **2021**, *50*, 259–275.
[15] Y. Zhu, J. Zhao, L. Li, J. Xu, X. Zhao, Y. Mi, J. Jin, *Dalton Trans.* **2021**, *50*, 10758–10764.
[16] S. Wen, J. Zhao, Y. Zhu, J. Mao, H. Wang, J. Xu, *J. Alloys Compd.* **2020**, *837*, 155536.
[17] Y. Zhang, S. Li, L. Cheng, Y. Li, X. Ren, P. Zhang, L. Sun, H. Y. Yang, *J. Mater. Chem. A* **2021**, *9*, 3388–3397.
[18] K. H. Nam, C. M. Park, *J. Mater. Chem. A* **2016**, *4*, 8562–8565.
[19] Y. Zhu, J. Zhao, L. Li, J. Mao, J. Xu, J. Jin, *Chem. Eng. Sci.* **2020**, *225*, 1–9.
[20] J. Ibers, *Nat. Chem.* **2009**, *1*, 508.
[21] Y. Chen, H. Fu, Y. Huang, L. Huang, X. Zheng, Y. Dai, Y. Huang, W. Luo, *ACS Materials Lett.* **2021**, *3*, 160–170.
[22] D. B. Miracle, O. N. Senkov, *Acta Mater.* **2017**, *122*, 448–511.
[23] Z. Fan, H. Wang, Y. Wu, X. J. Liu, Z. P. Lu, *RSC Adv.* **2016**, *6*, 52164–52170.
[24] M. N. Obrovac, V. L. Chevrier, *Chem. Rev.* **2014**, *114*, 11444–11502.
[25] J. Rodríguez-Carvajal, *Physica B: Condensed Matter* **1993**, *192*, 55–69.
[26] H. Kim, M. J. Kim, Y. H. Yoon, Q. H. Nguyen, I. T. Kim, J. Hur, S. G. Lee, *Electrochim. Acta* **2019**, *293*, 8–18.
[27] L. Li, J. Zhao, H. Zhao, J. Mao, *J. Alloys Compd.* **2022**, *920*, 166003.
[28] A. Wang, W. Hong, L. Li, R. Guo, Y. Xiang, Y. Ye, G. Zou, H. Hou, X. Ji, *Energy Storage Mater.* **2022**, *44*, 145–155.
[29] J. Chen, Z. Sun, Y. Zhu, N. Chen, Y. Zhou, J. Ding, X. Chen, L. Chen, *Dalton Trans.* **2011**, *40*, 340–343.
[30] T. Yang, J. Liu, D. Yang, Q. Mao, J. Zhong, Y. Yuan, X. Li, X. Zheng, Z. Ji, H. Liu, G. Wang, R. Zheng, *ACS Appl. Energ. Mater.* **2020**, *3*, 11073–11081.
[31] Y. Wei, J. Chen, S. Wang, X. Zhong, R. Xiong, L. Gan, Y. Ma, T. Zhai, H. Li, *ACS Appl. Mater. Interfaces* **2020**, *12*, 16264–16275.
[32] R. Jung, M. Metzger, D. Haering, S. Solchenbach, C. Marino, N. Tsiouvaras, C. Stinner, H. A. Gasteiger, *J. Electrochem. Soc.* **2016**, *163*, A1705–A1716.
[33] J. T. Li, J. Swiatowska, A. Seyeux, L. Huang, V. Maurice, S. G. Sun, P. Marcus, *J. Power Sources* **2010**, *195*, 8251–8257.
[34] J. T. Li, J. Światowska, V. Maurice, A. Seyeux, L. Huang, S. G. Sun, P. Marcus, *J. Phys. Chem. C* **2011**, *115*, 7012–7018.
[35] F. Liao, J. Światowska, V. Maurice, A. Seyeux, L. H. Klein, S. Zanna, P. Marcus, *Electrochim. Acta* **2014**, *120*, 359–368.
[36] L. Gehrlein, C. Njel, F. Jeschull, J. Maibach, *ACS Appl. Energ. Mater.* **2022**, *5*, 10710–10720.
[37] E. Markevich, G. Salitra, F. Chesneau, M. Schmidt, D. Aurbach, *ACS Energy Lett.* **2017**, *2*, 1321–1326.
[38] S. Hong, M. H. Choo, Y. H. Kwon, J. Y. Kim, S. W. Song, *Adv. Mater. Interfaces* **2016**, *3*, 22.
[39] K. Feng, M. Li, W. Liu, A. G. Kashkooli, X. Xiao, M. Cai, Z. Chen, *Small* **2018**, *14*, 1702737.
[40] T. Lu, S. Dong, C. Zhang, L. Zhang, G. Cui, *Coord. Chem. Rev.* **2017**, *332*, 75–99.

RESEARCH ARTICLE
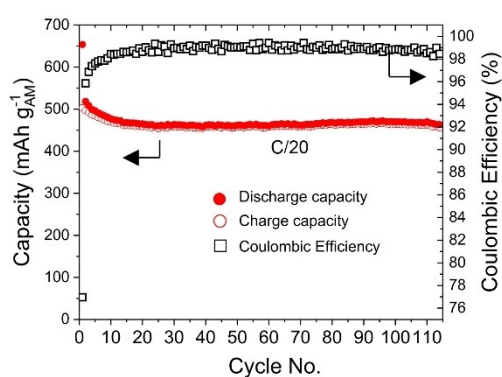
Dr. S. Alvi*, Dr. A. P. Black, I. Jozami, Dr. C. Escudero, Prof. F. Akhtar, Prof. P. Johansson

1 – 7

Entropy Stabilized Medium High Entropy Alloy Anodes for Lithium-ion Batteries

Improved battery cycling by alloy engineering: A medium high-entropy alloy, $BiSbSe_{1.5}Te_{1.5}$, is used to showcase how increased entropy can reduce the propensity of electrode pulverization and improve the cycling stability of conversion-alloying anodes – and this without compositing with any carbonaceous materials. The structural evolution of $BiSbSe_{1.5}Te_{1.5}$ during (de)lithiation is followed by *operando* X-ray diffraction.